



Microstructure and mechanical properties of electron beam welded TiZrNbTa refractory high entropy alloy

N. Li^{a,b}, R.X. Wang^c, H.B. Zhao^a, Y. Tang^{c,**}, P. Xue^{a,d}, D.R. Ni^a, B.L. Xiao^a, Z.Y. Ma^a, L. H. Wu^{a,d,*}

^a Shi-changxu Innovation Center for Advanced Materials, Institute of Metal Research, Chinese Academy of Sciences, 72 Wenhua Road, Shenyang 110016, China

^b School of Materials Science and Engineering, University of Science and Technology of China, 72 Wenhua Road, Shenyang 110016, China

^c Department of Materials Science and Engineering, College of Aerospace Science and Engineering, National University of Defense Technology, Changsha 410073, China

^d Key Laboratory of Nuclear Materials and Safety Assessment, Institute of Metal Research, Chinese Academy of Sciences, 72 Wenhua Road, Shenyang 110016, China

ARTICLE INFO

Keywords:

Refractory high entropy alloys
Electron beam welding
Microstructure
Mechanical properties

ABSTRACT

It is stringent to develop welding techniques for refractory high entropy alloys (RHEAs) to fabricate large-sized components, since it is difficult to fabricate large-sized RHEA castings because of their poor fluidity and severe element segregation. Here, we first time utilize electron beam welding (EBW) to join TiZrNbTa RHEA, and a defect-free joint is successfully achieved. After EBW, a coarse casting microstructure is largely refined with the reduction of casting porosities. The average hardness in the entire joint is almost uniform, which is the comprehensive effect between the weakening of solution strengthening and the grain refinement strengthening. The tensile strength of the joint achieves 940 MPa, with a high strength efficiency of 90%. This study provides a way to fabricate large-sized RHEA components.

1. Introduction

The refractory high entropy alloys (RHEAs) are a type of new materials containing refractory metals such as Ti, Zr, Nb, Ta, W, V, Mo, Hf, etc, which are developed on the basis of HEAs generally consisting of five or more elements with near-equiatomic concentrations [1,2]. The RHEAs exhibit high room temperature strength, excellent high temperature properties and corrosion resistance over the traditional Ni-based superalloys at an even higher service temperature [3–10]. Therefore, RHEAs show a great potential to apply in the aerospace field with extremely high servicing temperature requirement, since there are very little space on further improvement of the service temperature for the traditional aero engine materials, such as Ni-based superalloys [6]. Besides, RHEAs also show great potential application in nuclear fields since RHEAs also exhibit a very good irradiation property [11–14].

Although the RHEAs exhibit great potential of applying in aerospace and nuclear fields, the large-sized castings are still very difficult to fabricate. This is mainly limited by their poor fluidity and the tending of easily producing shrinkage porosities. Besides, the element segregation

especially easily occurs as the result of the effects of the mixing entropy, mixing enthalpy, electronegativity, valence electron concentration etc, which makes it more difficult to fabricate large-sized RHEA castings, and thus the application of RHEAs is largely limited [15–17].

Welding is a fast and often a reliable way to produce permanent and continuous joints. Therefore, welding technologies become unquestionably competitive for industrial sectors, such as infrastructure construction and transportation. It is well-known that large-sized components could be fabricated via the welding of several segments or parts together. In addition, most RHEAs have quite low ductility at room temperature, even under compression, so they can only be processed at high temperatures, but the processing is still rather difficult [9]. Therefore, it is very necessary and stringent to develop welding techniques for the RHEAs to fabricate large-sized RHEA components.

At present, the research on the welding for the RHEAs is very limited, because of its high melting point, poor fluidity and low thermal conductivity. Until now, only Panina et al. [18] reported the laser beam welding of Ti_{1.89}NbCrV_{0.56} RHEA. They found that the defect-free joint of the Ti_{1.89}NbCrV_{0.56} RHEA could not be achieved via the normal laser

* Corresponding author at: Shi-changxu Innovation Center for Advanced Materials, Institute of Metal Research, Chinese Academy of Sciences, 72 Wenhua Road, Shenyang 110016, China.

** Corresponding author.

E-mail addresses: tangyu15@zju.edu.cn (Y. Tang), lhwu@imr.ac.cn (L.H. Wu).

<https://doi.org/10.1016/j.mtcomm.2022.103847>

Received 4 February 2022; Received in revised form 23 May 2022; Accepted 13 June 2022

Available online 16 June 2022

2352-4928/© 2022 Elsevier Ltd. All rights reserved.

beam welding. The sound butt joints without cracks for the RHEA were achieved until using the preheating assisting system and by adjusting preheating temperature to over 600 °C before laser beam welding. However, the preheating welding process largely increases the complexity and difficulty of welding. Therefore, it is of great significance to further explore different welding techniques of RHEAs.

Among different welding methods, electron beam welding (EBW) has been widely used in the traditional materials [19,20], and high entropy alloys [21] because of its high energy density, fast welding speed, good controllability and low oxidation resistance under vacuum condition, and the great advantage on the joining quality has been proved [22–25]. For example, an autogenously dissimilar Al0.1CoCrFeNi HEA / stainless steel weld joint was produced by EBW, and the equal strength welding was achieved [21]. Therefore, it might be a good way to develop EBW on the RHEAs in order to further expand the application of the RHEAs.

In this study, the TiZrNbTa RHEA was selected as the typical RHEA material since it has great potential to be used as high temperature materials due to its superior high temperature properties (e.g. its compression yield strength of 813 MPa at 600 °C, and 410 MPa even at 1000 °C) [26–29]. The TiZrNbTa RHEA was joined by EBW, and the microstructure and mechanical properties were investigated. While the microstructure mechanism of the electron beam welded joint were discussed, and the feasibility of the RHEA welding was proved.

2. Materials and experimental methods

The raw materials were 20 mm × 20 mm × 3 mm as-cast TiZrNbTa RHEA plates prepared by arc melting. The EBW equipment with EB4C-150–15-W of the PACAC was used to weld the TiZrNbTa RHEA plates. Referring to our EBW welding experience, and the welding parameters of titanium alloys [30,31] and HEAs [32,33], the welding parameter of the TiZrNbTa RHEA was set as follows: the plates were joined by EBW in vacuum conditions of 1×10^{-4} Pa, with the welding parameters of the voltage of 120 kV, the electron beam of 13 mA, and the welding speed of 800 mm/min. After welding, the sample was kept in vacuum for 15 min and then air-cooled. The microstructure of the base material (BM), the

heat-affected zone (HAZ) and the fusion zone (FZ) was analyzed by x-ray diffraction (XRD), with the scanning angle of XRD of 20–80°.

Metallographic samples were taken from the joint vertical to welding direction. The samples were etched with a mixture of hydrofluoric acid, nitric acid and water before metallographic observation. The phase composition, microporosity and the fracture samples were characterized by scanning electron microscopy (SEM) with energy dispersive spectroscopy (EDS). The grain size, grain boundary and orientation difference were analyzed by electron backscatter diffraction (EBSD). FM-700 microhardness tester was used to measure Vickers hardness with the load of 500 g and the holding time of 15 s. The gauge length, width and thickness of the tensile specimens were 10 mm, 1.5 mm and 1 mm, respectively. To ensure the experimental accuracy, three tensile specimens were prepared, and the strain rate for tension was 1×10^{-3} s⁻¹. The sample size of the SEM and EBSD was 20 × 3 × 2 mm³.

3. Results and discussion

3.1. Microstructure analysis

Fig. 1 shows the macroscopic surface topography of the EBW TiZrNbTa RHEA. It is found that the surface of the FZ is well formed without macroscopic defects such as pores and cracks (Fig. 1a). At the bottom of the weld, there are some bulges, which are mainly caused by a small amount of collapse of the molten metal under gravity with the high-speed impact of the electron beam during the welding process. The silvery white area about 3 mm wide on either side of the FZ should be the metallic vapor, which is the result of the metal evaporation of the FZ during the EBW process. The metal vapor might mainly consist of Ti and Zr elements. The melting point of the Ti is the lowest among the four elements, only 1668 °C, while the Zr shows slightly higher melting point than the Ti, but Zr element has higher mixing enthalpy and diffusion rate [28]. Therefore, the Ti element and the Zr element should evaporate more easily.

Fig. 2 shows the metallographic structure of the cross-sectional joint. The width of the FZ is about 1.4 mm, and the width of the upper part of

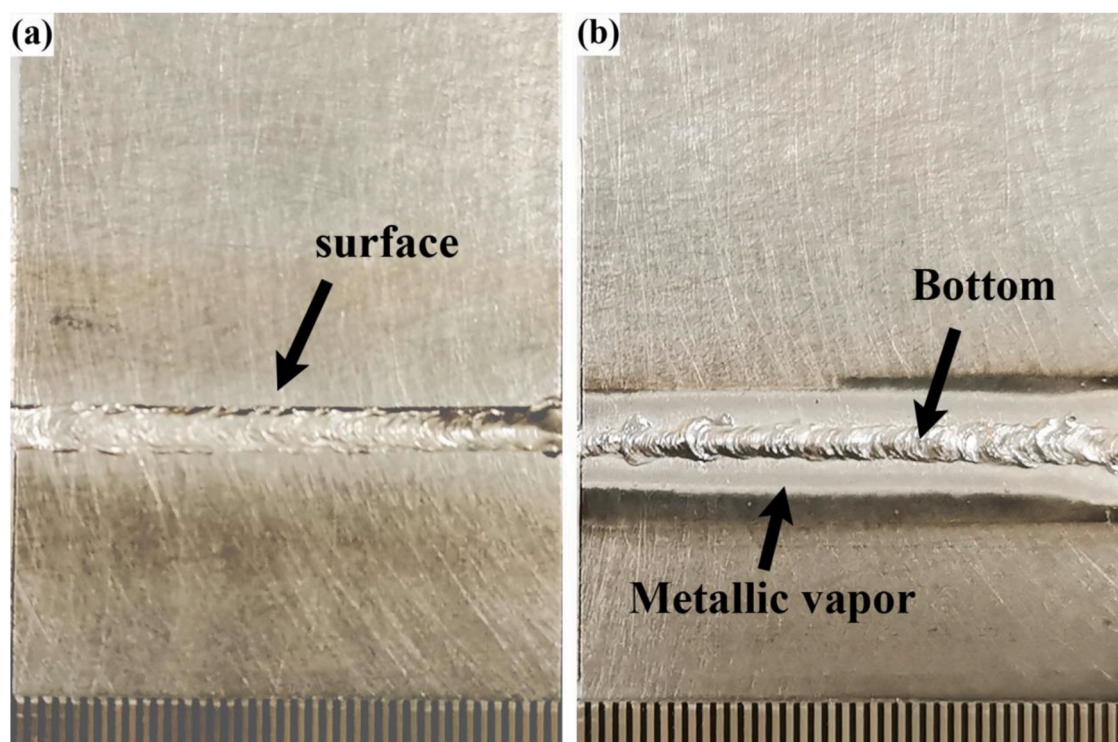


Fig. 1. Macroscopic surface morphologies of EBW at: (a) upper surface, (b) bottom.

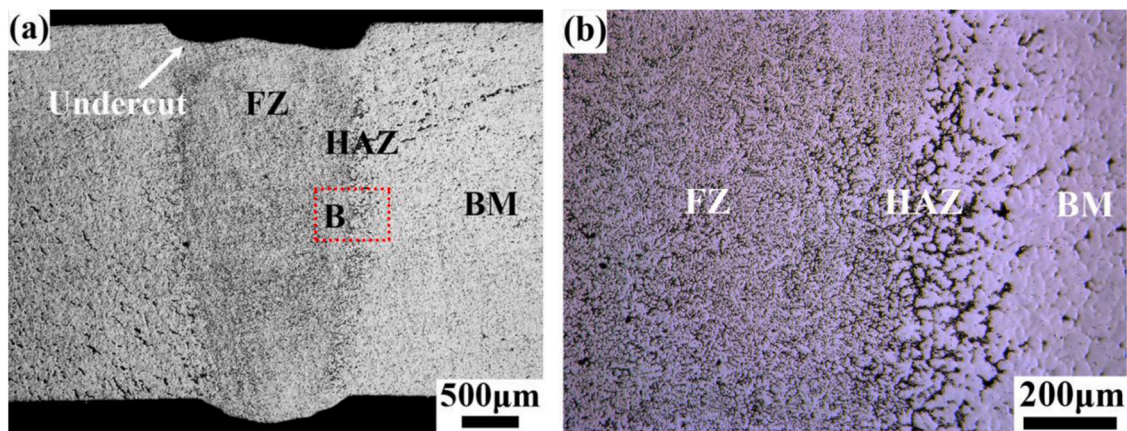


Fig. 2. Metallographic structure of welded joint: (a) cross-sectional macrostructure, (b) magnified image of zone B in (a).

the FZ is slightly larger than that of the bottom part (Fig. 2a). It results from the high energy density of the EBW, where the weld seam with large aspect ratio is generally obtained [34]. Besides, it is found that the joint can be divided into three zones, i.e. the FZ, the zone undergoing melting and subsequent solidification; the HAZ, the zone experiencing thermal cycling but not melting; and BM, the zone unaffected by heat.

A welding undercut with a depth of about 200 μm is found on the upper surface of the joint, and this is caused by excessive welding heat input, which can be eliminated by reducing the heat input. For a 3 mm thick plate, only 200 μm undercut is found after welding, which is almost negligible in engineering applications. A small surplus height of seam is found at the bottom, and the main reason is that the melted metal collapses due to the influence of gravity, as the result of the absence of a backing plate at the bottom.

The magnified image in Fig. 2b shows that the FZ, HAZ and BM can be more clearly distinguished. Compared with the BM and HAZ, the grain size of the FZ is obviously refined. This is because the rapid cooling of the FZ causes no enough time for the grains in the FZ to grow. It can also be seen from Fig. 2b that the width of the HAZ is about 200 μm . It is mainly due to the high speed of EBW and high energy density, which leads to small or even no HAZ. For example, Sokkalingam et al. [21] performed EBW on HEA and stainless steel, and no HAZ was found at the welded joint. This is different from traditional fusion welding with a low energy density and a large width of HAZ. For example, the width of about 1 mm for the HAZ was found after GTAW Ti alloy [35]. Besides, No cracks and other defects are found in the FZ after EBW. Therefore, it is proved to be feasible for the EBW applied for the TiZrNbTa RHEA.

As is mentioned in the Section 1, it is not easy to welding the RHEAs. In this study, the weldability of the TiZrNbTa RHEA should be mainly attributed to two aspects. On one hand, although the TiZrNbTa RHEA has poor fluidity, the flow of the welding pool can be improved by EBW with high energy density. On the other hand, the vacuum environment for EBW is very benefit for the success of welding, since it is not only conducive to expel the initial pores in the casting, but also can effectively avoid the reaction of elements in the TiZrNbTa RHEA (especially for the elements which are very sensitive to atmosphere, such as Ti and Nb) with hydrogen, oxygen and nitrogen elements in the atmosphere.

Fig. 3 shows the XRD results of the BM, HAZ and FZ. It is found that the BM, HAZ and FZ all consist of a single BCC structure. The lattice constant of all different zones is 0.3296 nm, which is close to the lattice constant of pure Ta with BCC structure ($a=0.3330$ nm). Nguyen et al. [28] performed XRD analysis on the as-cast TiZrNbTa RHEA and found that the as-cast TiZrNbTa RHEA also exhibited a single BCC structure, but the segregation of Zr element was found by EDS of both SEM and transmission electron microscopy (TEM). Therefore, although the XRD results showed that the BM, HAZ and FZ consist of a single BCC structure, the segregation of Zr element is also found in the subsequent EDS

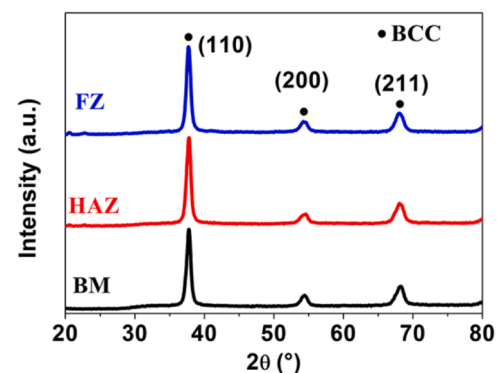


Fig. 3. XRD patterns of BM, HAZ and FZ in joint.

experiments, which will be analyzed later. Actually, Liu et al. [26] found the existence of the second phase by Lorentz function fitting of the XRD results of the as-cast TiZrNbTa RHEA.

In order to further explore the microstructure of the BM, HAZ and FZ, the elemental distribution in the dendrite (DR) and inter-dendrite (ID) of the different regions was examined by EDS, and the typical chemical compositions with the atomic percentage in the different regions are listed in Table 1. The most distributed elements in the DR are Ta and Nb elements, while the Zr element is mostly distributed in the ID (>35%). In addition, the distribution of the Ti element is relatively uniform.

Fig. 4 shows the SEM and EDS mapping images in the different zones of the joint. It is obvious that the segregation of the Zr element occurs in different zones of the joint. There are two main reasons for this. On one hand, the higher mixing enthalpy between Zr and Nb or Ta tends to cause the increase of Gibbs free energy (Table 2). In order to reduce the free energy of the material and obtain a relatively stable alloy system, the Zr element is segregated. This phenomenon is consistent with the reason for Cu segregation at grain boundaries in CoCrFeNiCu HEA reported by our previous study [36].

Table 1

Typical chemical composition of different regions of the joint in atomic percentage.

Region		Ti	Zr	Nb	Ta
BM	DR	21.35	20.65	29.77	28.22
	ID	26.13	35.33	22.13	15.36
HAZ	DR	20.61	19.69	29.94	29.76
	ID	27.33	38.74	21.08	12.85
FZ	DR	18.93	16.14	32.07	32.86
	ID	26.33	36.27	22.33	15.08

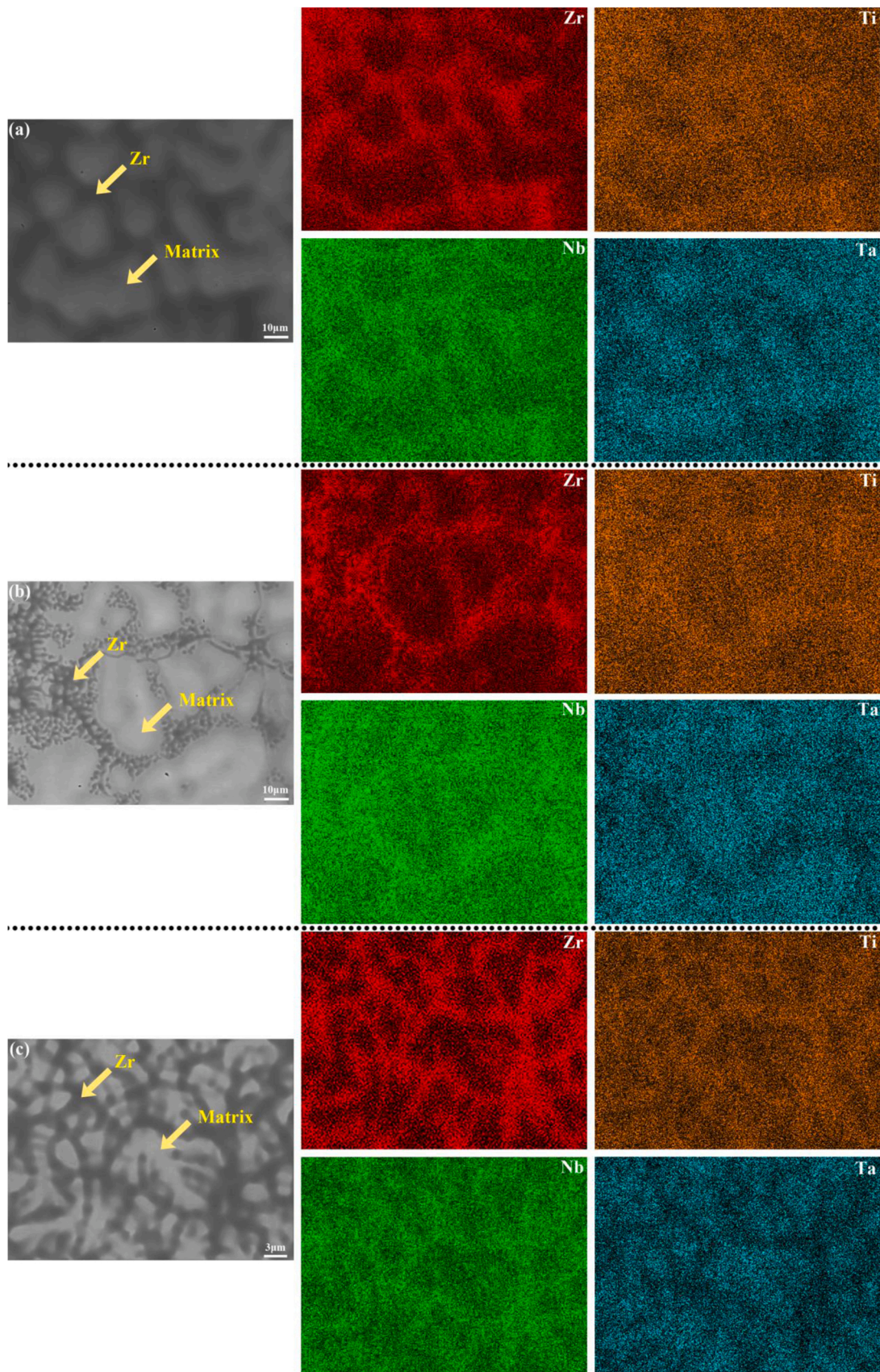


Fig. 4. SEM images and element distribution in different zones of joint: (a) BM, (b) HAZ, (c) FZ.

Table 2
Mixing enthalpy of each pair in TiZrNbTa HEA [28,37,38].

Mixing enthalpy (kJ/mol)	Ti	Zr	Nb	Ta
Ti	/	0	2	1
Zr	0	/	4	3
Nb	2	4	/	0
Ta	1	3	0	/

On the other hand, the diffusion rate of Zr element is 3–4 orders of magnitude higher than that of Ti, Nb and Ta [28], which means that Zr element is able to segregate faster at the grain boundary during the process of the melting and solidification of HEA materials. This experimental result has been confirmed by Nguyen et al. [28] through the combination of simulation and experiment results. According to the overall morphology of the FZ (Fig. 4c), based on the different contrast degree between the matrix phase and the Zr-rich phase, the morphology of the FZ is a typical dendritic morphology, and the Zr-rich phases locate at dendritic boundaries.

The dendritic structure formed in the FZ is quite different from those in the BM and HAZ. The FZ re-melts during EBW and has a large cooling rate. The large negative temperature gradient leads to the formation of dendritic structure in the FZ. In this process, the different diffusion rates of the elements lead to the redistribution of the elements in phases, while the Zr element diffuses rapidly at high temperature. Therefore, the matrix phase and the Zr-rich phase are formed in the DR and ID, respectively.

By comparing the microstructure in the BM and HAZ (Fig. 4a and b),

it can be found that the grain size in the two zones is similar, and only the morphology of the phase is slightly different. This is because the thermal influence of the HAZ leads to the secondary diffusion of the Zr element in the welding process. This is also confirmed by the point and line appearance of the Zr-rich phase in Fig. 4b. The heat in the HAZ is low and the cooling rate is fast, and thus the Zr element has not been fully diffused enough. As a result, the Zr-rich phase with a special point and line morphology is formed in the HAZ.

The segregation phenomenon of the Zr-rich phase can be analyzed by the Table 1. The content of Zr in the matrix phase in the FZ is the lowest. On one hand, it might be attributed to that the metal in the FZ is re-melted, and the Zr element is re-distributed in the matrix. On the other hand, Zr element of the FZ evaporates on the surface to form metallic vapors (Fig. 1). Therefore, the Zr element in the matrix phase of the BM is slightly higher than that in the FZ. The difference of Zr content also explains the difference of the corrosion contrast in the BM and HAZ in Fig. 2b.

Besides, a number of black points are found in the BM, HAZ and FZ (Fig. 5). These black points (indicated by the arrows) should be pores. Such kind of pores exists for as-cast RHEAs in this study and also in other RHEAs reported in the previous studies, such as MoNbHfZrTi [39] and AlMoTaTiZr [40]. The reason should be attributed to two aspects. On one hand, the different melting points of the elements in the RHEAs lead to the different solidification sequence of the elements, and thus it is easy to form pores. On the other hand, oxygen and nitrogen absorbed during alloy dissolution are released during solidification, resulting in casting shrinkage. In addition, compared to traditional alloys, RHEAs are more likely to form pores during solidification due to its poor

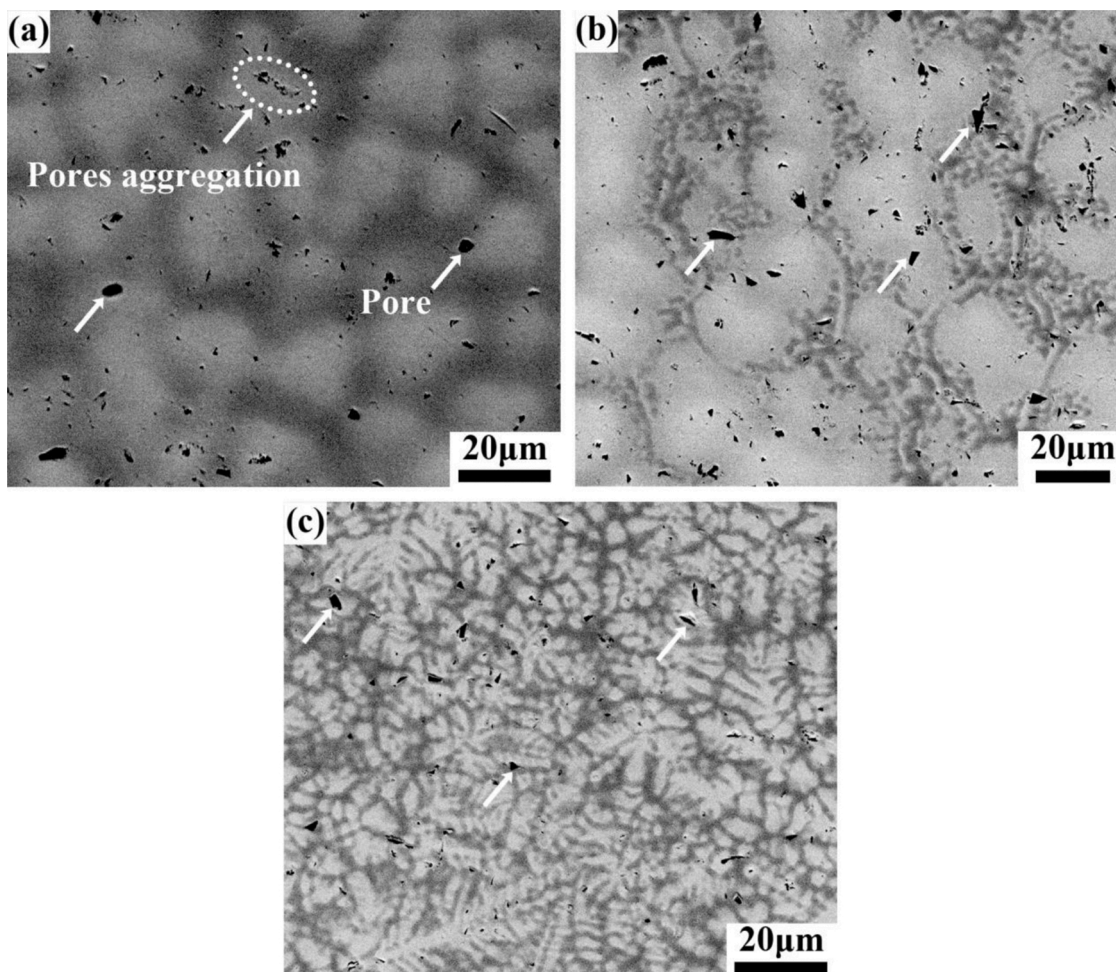


Fig. 5. SEM images of different zones in joint: (a) BM, (b) HAZ, (c) FZ.

fluidity. The pore causes local stress concentration in the material and becomes the source of cracks. Especially in the form of small pore aggregation, it not only increases the sensitivity of notch and reduces the strength, but also easily reduces the fatigue property of the material.

From Fig. 5a, the pore size in the BM is about 5.5 μm and the small pores aggregation can be found in the BM. After EBW, the pore size decreases significantly (about 3.1 μm) and the small pore aggregation disappears in the FZ. According to the statistical results, the microporosity of the BM, HEA and FZ is 0.61%, 0.67% and 0.36%, respectively. This is because of the re-melting of the material during welding, and the faster cooling in the FZ making the pores not easy to form and grow. Besides, EBW under the vacuum environment is more conducive to expel pores. Compared with the pore aggregation of the BM, the uniform distribution of the pores of the FZ is more conducive to reducing stress concentration.

Fig. 6 shows an EBSD diagram of the entire joint. After EBW, the grain is largely refined in the FZ compared to that of the BM. This is the result of the rapid cooling of the metal in the FZ, which is consistent with

the result in Fig. 2. Besides, most of the grains in the FZ are equiaxed grains. The grain size distribution diagram in Fig. 6c and d shows that the average grain size of the BM is 56 μm, while the grain size of the FZ is 26 μm. Furthermore, the misorientation angle distribution in Fig. 6e and f shows that the proportion of high angle grain boundary in the BM and FZ is 44% and 69%, and that of the twin boundary is 5.6% and 5.2%, respectively (The black line and the green line represent the high angle grain boundary and the low angle grain boundary, respectively).

3.2. Mechanical properties

Fig. 7 shows the tensile properties of the BM and the joint, and the typical fracture surface of the welded joint. The yield strength (YS) and the ultimate tensile strength (UTS) of the BM are 911 ± 9 MPa and 1040 ± 18.7 MPa, respectively. The average elongation of the BM is about 6% ± 5.1% (Fig. 7b). It is worth noting that the elongation of the BM fluctuates greatly, which is caused by the non-uniform structure with many casting pores as the result of poor fluidity of the BM. In the

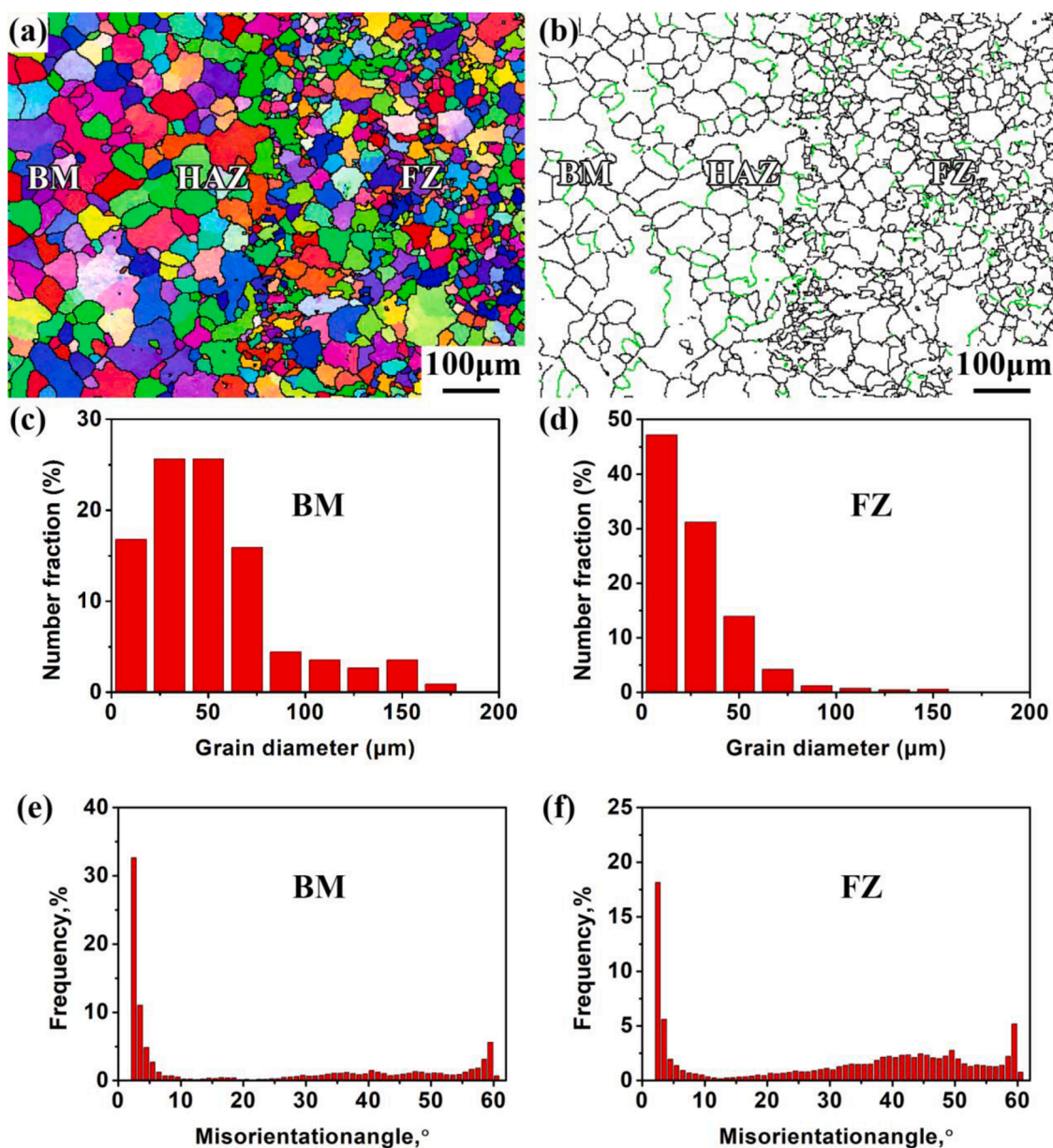


Fig. 6. EBSD diagram of joint: (a) EBSD orientation map, (b) grain boundary map, (c) (d) grain size distribution map in BM and FZ, and (e) (f) misorientation distribution map in BM and FZ.

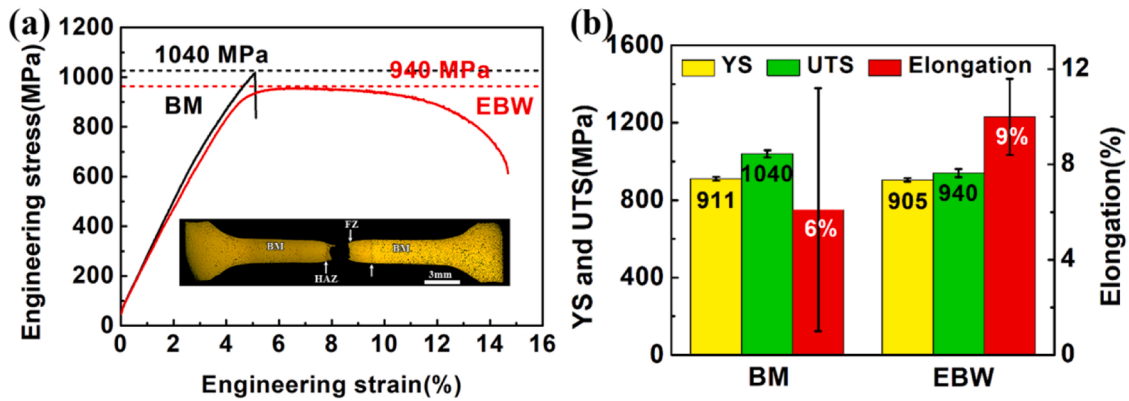


Fig. 7. Tensile properties of BM and welded joint; (a) the typical tensile curve and (b) the average tensile properties.

BM, it is very easy to form casting pores, which has been shown in Fig. 6. When the BM contains some large casting pores, it will show the brittle fracture (the typical tensile curve is shown in Fig. 7a). While the BM containing less or even no casting pores shows a large elongation. Thus, the elongation of the BM fluctuates largely. In contrast, the mechanical property of the FZ is more uniform. The YS and the UTS of the entire welded joint are 905 ± 9 MPa and 940 ± 21.2 MPa, but the elongation increases to about $9\% \pm 1.6\%$. This indicates that the vacuum environment for EBW can improve the as-cast microstructure defects, thereby improving the ductility. The coefficient of the welded joint refers to the ratio of the welded joint strength to the BM strength. Therefore, the joint coefficient of TiZrNbTa RHEA welded by EBW is 90%.

The coefficient of the welded joint is commonly used to indicate the reliability of weld quality in engineering. Such a high strength coefficient means that it can be used as a key part of the bearing structure in engineering applications. This indicates the feasibility of EBW applied for the TiZrNbTa RHEA. The fracture of the welded joint occurs in the FZ, and the typical macro morphology of the fracture position of the welded joint is shown at the bottom of Fig. 7a. The increase of the elongation for the joint should be related to that the main deformation occurring in the FZ rather than the BM.

The current mechanical properties are compared with reported data of similar composition [8,26,27], and the related results are shown in the Table 3. It is obvious that the strength of RHEAs with TiZrNbTa or similar compositions is about 900–1200 MPa, and the relevant literatures are almost about the compressive properties of the RHEAs, but there are few reports about the tensile properties from the Table 3. As we know, compared with compression properties, tensile properties can better represent the performance properties in the engineering applications, especially the materials with the poor ductility, such as RHEAs. Therefore, in this study, the tensile properties of the RHEAs can provide a good reference for the engineering application. In addition, the joint coefficient of 90% indicates that the EBW is an effective method of producing large-area RHEAs with excellent mechanical properties.

Fig. 8 shows the overall hardness diagram of the welded joint. The average hardness of the BM, HAZ and FZ is 302 ± 5 HV. This result is

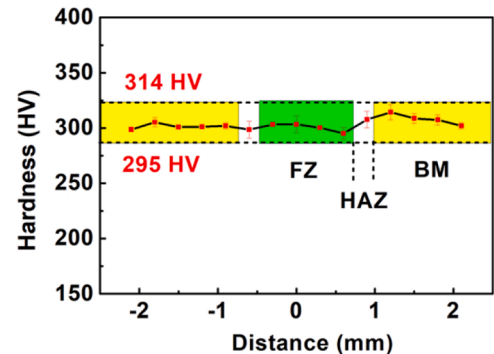


Fig. 8. Vickers hardness distribution through welded joint.

consistent with the similar yield strength of the BM and the FZ. The SEM and EBSD results have showed that the grain size of the FZ is significantly refined. Generally, the grain refinement might improve the strength and hardness of the material. However, the hardness of the FZ is almost unchanged compared to that of the BM. It means that other strengthening effects for the refined grains in the FZ must be weakened.

It is well known that the mechanical properties of materials are mainly affected by the following strengthening mechanisms: solid solution strengthening, grain boundary strengthening, dislocations strengthening and precipitate strengthening. In this study, the mechanical properties of the BM and FZ should be affected by solid solution strengthening and grain boundary strengthening.

The grain size in the BM and FZ is largely different. The relationship between the YS and the grain size could be described by Hall-Petch.

$$\sigma_y = \sigma_0 + k_y d^{-1/2}$$

Where σ_y is the YS, σ_0 is again the lattice friction stress, d is the average grain size and k_y is the Hall-Petch relationship coefficient. The YS increase caused by grain size difference ($\Delta\sigma$) can be expressed as:

$$\Delta\sigma = k_y (d_{FZ}^{-1/2} - d_{BM}^{-1/2})$$

Where the d_{FZ} is the average grain size of the FZ (26 μm), and the d_{BM} is the average grain size of the BM (56 μm). The k_y value of the HEA is about 450–700 MPa $\text{mm}^{1/2}$ [41–43]. Therefore, the strength enhancement caused by grain boundary strengthening in the FZ (compared with the BM) is about 28.1–43.8 MPa. This indicates that although the grain size of the FZ is significantly refined, the strength effect is not significant.

According to the rule of mixture (ROM) of the RHEA, the calculated values (294 MPa) are much smaller than the measured values (911/940 MPa) of the TiZrNbTa RHEA. This result has been confirmed in the TiNbTaV, NbTaVW and TiNbTaVW [44,45]. This indicates that the solid solution strengthening plays a more important role in the TiZrNbTa RHEA than the simple rule of mixture [46–48]. In this study, compared with the BM, the Zr element in the DR of the FZ decreases to some extent,

Table 3
Compressive/tensile strength of RHEAs with similar composition [8,26,27].

Alloy	Condition	YS (MPa)	Property	Ref.
NbTiZr	As-cast	975	Compressive strength	[8]
NbTiZrV	As-cast	1110	Compressive strength	[8]
TiZrNbTa	As-cast	957	Compressive strength	[26]
TiZrNbTa	As-homogenized	1220	Compressive strength	[26]
TiZrNbTa	As-cast	1100	Compressive strength	[27]
TiZrNbTa	As-cast	940	Tensile strength	This study
TiZrNbTa	welded	905	Tensile strength	This study

while the Zr element in the ID of the FZ increases slightly (Table 1). This means that the secondary diffusion and evaporation of the Zr elements result in the weakening of solid solution strengthening in the FZ. However, the evaporation and diffusion of the elements are difficult to quantify, the degree of the FZ weakening cannot be calculated. But, the hardness is evenly distributed under the comprehensive effect of two strengthening mechanisms. Therefore, the strength of the FZ might be reduced with a small extent (with the similar extent with the grain refinement strengthening) via the loss of the solution strengthening. The analysis results are similar to those reported by Sokkalingam et al. [49]. They found that after welding, the grain size in the FZ of Al0.5CoCrFeNi HEA was significantly refined, but the strength and hardness were reduced. It was attributed to that the decrease of beta phase and twin fraction weakened the strengthen effect.

Fig. 9 shows the fracture morphology of the BM and the joint. The BM mainly exhibits an intergranular fracture mode, and some cracks are found at grain boundaries (Fig. 9a and b), which explains the cause of the low elongation for the BM. Different from the BM, the joint exhibits an obvious necking characteristic during the tensile process, and a large number of dimples can be found (Fig. 9c and d). Therefore, the joint shows the obviously ductile fracture mode. It suggests that ductile fracture takes place in the FZ with a finer microstructure, totally different from the brittle fracture mode in the BM. That is why the elongation of the joint even increases compared to that of the BM.

Therefore, in this study, the weldability of TiZrNbTa HEA is explored using the EBW. A defect-free welded joint is obtained successfully for the first time, and the elongation of the joint is improved while the high strength is maintained. The high joint coefficient of 90% suggests that

the EBW is of great potential to fabricate large sized RHEA component. However, for the engineering application, more systematic and deep investigations should be made on the EBW of RHEAs in the future.

4. Conclusions

- 1) For the first time, the EBW technology is used for TiZrNbTa RHEA to achieve the defect-free welded joint, and the welding joint coefficient reaches 90%.
- 2) After EBW, the grain is largely refined, and the casting pores are largely reduced in the FZ compared to those of the BM.
- 3) Compared with that of the BM, the grain size of the FZ is significantly refined, but the hardness in the FZ shows no obvious change. The main reason comes from the comprehensive effect between the weakening of solution strengthening of Zr element and the grain refinement strengthening in the FZ.

CRediT authorship contribution statement

N. Li: Investigation, Data curation, Writing – original draft. **R.X. Wang:** Investigation, Validation. **H.B. Zhao:** Investigation, Methodology. **Y. Tang:** Resources, Visualization. **P. Xue:** Conceptualization, Methodology. **D.R. Ni:** Conceptualization, Project administration. **B.L. Xiao:** Visualization, Supervision. **Z.Y. Ma:** Resources, Supervision. **L.H. Wu:** Conceptualization, Funding acquisition, Writing – review & editing.

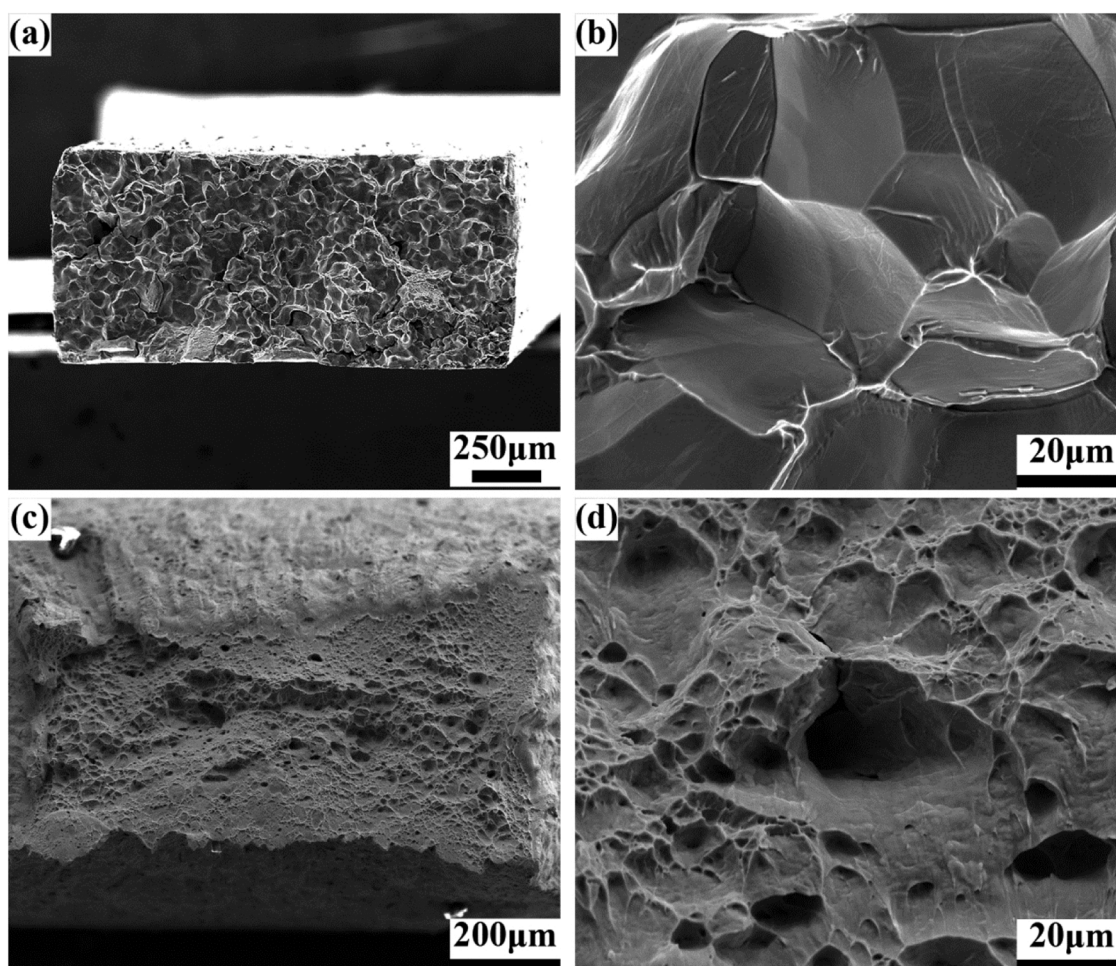


Fig. 9. Fracture morphology of BM and joint: (a) (b) fracture morphology of BM, (c) (d) fracture morphology of joint.

Declaration of Competing Interest

The authors declare that they have no known competing financial interests or personal relationships that could have appeared to influence the work reported in this paper.

Acknowledgments

This work was supported by the Youth Innovation Promotion Association of the Chinese Academy of Sciences (2021193 and Y2021061), and the National Natural Science Foundation of China under Grant No. U20A20231.

References

- [1] Y. Zhang, X. Yang, P.K. Liaw, Alloy design and properties optimization of high-entropy alloys, *JOM* 64 (7) (2012) 830–838.
- [2] O.N. Senkov, G.B. Wilks, D.B. Miracle, C.P. Chuang, P.K. Liaw, Refractory high-entropy alloys, *Intermetallics* 18 (9) (2010) 1758–1765.
- [3] Z. Lei, X. Liu, Y. Wu, H. Wang, S. Jiang, S. Wang, X. Hui, Y. Wu, B. Gault, P. Kontis, D. Raabe, L. Gu, Q. Zhang, H. Chen, H. Wang, J. Liu, K. An, Q. Zeng, T.-G. Nieh, Z. Lu, Enhanced strength and ductility in a high-entropy alloy via ordered oxygen complexes (563, 2018, p. 546, 2018), *Nature*, 565(7739), 2019, pp. E8–E8.
- [4] O.N. Senkov, S.V. Senkova, D.B. Miracle, C. Woodward, Mechanical properties of low-density, refractory multi-principal element alloys of the Cr-Nb-Ti-V-Zr system, *Mater. Sci. Eng. A Struct. Mater. Prop. Microstruct. Process.* 565 (2013) 51–62.
- [5] Y. Shi, B. Yang, P.K. Liaw, Corrosion-resistant high-entropy alloys: a review, *Metals* 7 (2) (2017).
- [6] V. Soni, O.N. Senkov, B. Gwalani, D.B. Miracle, R. Banerjee, Microstructural design for improving ductility of an initially brittle refractory high entropy alloy, *Sci. Rep.* 8 (2018).
- [7] M. Todai, T. Nagase, T. Hori, A. Matsugaki, A. Sekita, T. Nakano, Novel TiNbTaZrMo high-entropy alloys for metallic biomaterials, *Scr. Mater.* 129 (2017) 65–68.
- [8] O.N. Senkov, S. Rao, K.J. Chaput, C. Woodward, Compositional effect on microstructure and properties of NbTiZr-based complex concentrated alloys, *Acta Mater.* 151 (2018) 201–215.
- [9] O.N. Senkov, G.B. Wilks, J.M. Scott, D.B. Miracle, Mechanical properties of Nb₂₅Mo₂₅Ta₂₅W₂₅ and V₂₀Nb₂₀Mo₂₀Ta₂₀W₂₀ refractory high entropy alloys, *Intermetallics* 19 (5) (2011) 698–706.
- [10] O.N. Senkov, S.V. Senkova, C. Woodward, Effect of aluminum on the microstructure and properties of two refractory high-entropy alloys, *Acta Mater.* 68 (2014) 214–228.
- [11] Y. Lu, H. Huang, X. Gao, A promising new class of irradiation tolerant materials: Ti₂ZrHfV_{0.5}Mo_{0.2} high-entropy alloy, *J. Mater. Sci. Technol.* 35 (3) (2019) 369–373.
- [12] M. Sadeghilarijani, A. Ayyagari, S. Muskeri, Ion irradiation response and mechanical behavior of reduced activity high entropy alloy, *J. Nucl. Mater.* 529 (2020), 151955.
- [13] O. El-Atwani, N. Li, M. Li, Outstanding radiation resistance of tungsten-based high-entropy alloys, *Sci. Adv.* 5 (3) (2019).
- [14] T. Egami, W. Guo, P.D. Rack, Irradiation resistance of multicomponent alloys, *Metall. Mater. Trans. A Phys. Metall. Mater. Sci.* 45A (1) (2014) 180–183.
- [15] S. Guo, Q. Hu, C. Ng, C.T. Liu, More than entropy in high-entropy alloys: forming solid solutions or amorphous phase, *Intermetallics* 41 (2013) 96–103.
- [16] S. Guo, C. Ng, J. Lu, C.T. Liu, Effect of valence electron concentration on stability of fcc or bcc phase in high entropy alloys, *J. Appl. Phys.* 109 (10) (2011).
- [17] A. Takeuchi, A. Inoue, Quantitative evaluation of critical cooling rate for metallic glasses, *Mater. Sci. Eng. A Struct. Mater. Prop. Microstruct. Process.* 304 (2001) 446–451.
- [18] E. Panina, N. Yurchenko, S. Zherebtsov, N. Stepanov, G. Salishchev, V. Ventzke, R. Dinse, N. Kashaev, Laser beam welding of a low density refractory high entropy alloy, *Metals* 9 (12) (2019).
- [19] H. Liu, J. Song, H. Wang, Y. Du, K. Yang, Y. Liu, Q. Wang, Q. Chen, Heterogeneous microstructure and associated mechanical properties of thick electron beam welded Ti-5Al-25Sn-2Zr-4Mo-4Cr alloy joint, *Mater. Sci. Eng. A Struct. Mater. Prop. Microstruct. Process.* 825 (2021).
- [20] R. Xu, F. Li, X. Zhao, W. Yan, Y. Zhang, C. Yuan, Joint strengthening mechanism in electron beam welding of Al/Cu bilayer laminated composite using double-sided method, *J. Mater. Eng. Perform.* 30 (8) (2021) 6355–6363.
- [21] R. Sankalingam, P. Mastanaiah, V. Muthupandi, K. Sivaprasad, K.G. Prashanth, Electron-beam welding of high-entropy alloy and stainless steel: microstructure and mechanical properties, *Mater. Manuf. Process.* 35 (16) (2020) 1885–1894.
- [22] G. Chen, J. Liu, Z. Dong, X. Shu, B. Zhang, Underlying reasons of poor mechanical performance of thick plate aluminum-copper alloy vacuum electron beam welded joints, *Vacuum* 182 (2020).
- [23] L. Li, S. Wang, W. Huang, Y. Jin, Microstructure and mechanical properties of electron beam welded TC4/TA7 dissimilar titanium alloy joint, *J. Manuf. Process.* 50 (2020) 295–304.
- [24] Y. Lu, R. Turner, J. Brooks, H. Basoalto, Microstructural characteristics and computational investigation on electron beam welded Ti-6Al-4 V alloy, *J. Mater. Process. Technol.* 288 (2021).
- [25] I. Magnabosco, P. Ferro, F. Bonollo, L. Arnberg, An investigation of fusion zone microstructures in electron beam welding of copper-stainless steel, *Mater. Sci. Eng. A Struct. Mater. Prop. Microstruct. Process.* 424 (1–2) (2006) 163–173.
- [26] T.-Y. Liu, J.C. Huang, W.-S. Chuang, H.-S. Chou, J.-Y. Wei, C.-Y. Chao, Y.-C. Liao, J.S.C. Jang, Spinodal decomposition and mechanical response of a TiZrNbTa high-entropy alloy, *Materials* 12 (21) (2019).
- [27] V.T. Nguyen, M. Qian, Z. Shi, T. Song, L. Huang, J. Zou, A novel quaternary equiatomic Ti-Zr-Nb-Ta medium entropy alloy (MEA), *Intermetallics* 101 (2018) 39–43.
- [28] V.T. Nguyen, M. Qian, Z. Shi, X.Q. Tran, D.M. Fabijanic, J. Joseph, D.D. Qu, S. Matsumura, C. Zhang, F. Zhang, J. Zou, Cuboid-like nanostructure strengthened equiatomic Ti-Zr-Nb-Ta medium entropy alloy, *Mater. Sci. Eng. A Struct. Mater. Prop. Microstruct. Process.* 798 (2020).
- [29] M. Niinomi, Fatigue performance and cyto-toxicity of low rigidity titanium alloy, Ti-29Nb-13Ta-4.6Zr, *Biomaterials* 24 (16) (2003) 2673–2683.
- [30] T. Pasang, J.M. Sanchez Amaya, Y. Tao, M.R. Amaya-Vazquez, F.J. Botana, J.C. Sabol, W.Z. Misiolek, O. Kamiya, Comparison of Ti-5Al-5V-5Mo-3Cr welds performed by laser beam, electron beam and gas tungsten arc welding, in: *Proceedings of the 5th Manufacturing Engineering Society International Conference (MESIC)*, Univ Zaragoza, Zaragoza, Spain, 2013, pp. 397–404.
- [31] J. Kar, S.K. Roy, G.G. Roy, Influence of beam oscillation in electron beam welding of Ti-6Al-4V, *Int. J. Adv. Manuf. Technol.* 94 (9–12) (2018) 4531–4541.
- [32] Z. Wu, S.A. David, Z. Feng, H. Bei, Weldability of a high entropy CrMnFeCoNi alloy, *Scr. Mater.* 124 (2016) 81–85.
- [33] R. Sankalingam, P. Mastanaiah, V. Muthupandi, K. Sivaprasad, K.G. Prashanth, Electron-beam welding of high-entropy alloy and stainless steel: microstructure and mechanical properties, *Mater. Manuf. Process.* 35 (16) (2020) 1885–1894.
- [34] J. Long, L.-J. Zhang, L.-L. Zhang, J. Ning, M.-X. Zhuang, J.-X. Zhang, S.-J. Na, Analysis of heterogeneity of fatigue properties of double-sided electron beam welded 140-mm thick TC4 titanium alloy joints, *Int. J. Fatigue* 142 (2021).
- [35] Q. Liu, W. Long, L. Fu, Z. Zhang, S. Zhong, H. Yang, Microstructure and mechanical properties of hydrogenated Ti-0.3Mo-0.8Ni alloy gas tungsten arc welding joints, *J. Mater. Eng. Perform.* 30 (2) (2021) 1022–1029.
- [36] N. Li, C.-L. Jia, Z.-W. Wang, L.-H. Wu, D.-R. Ni, Z.-K. Li, H.-M. Fu, P. Xue, B.-L. Xiao, Z.-Y. Ma, Y. Shao, Y.-L. Chang, Achieving a high-strength CoCrFeNiCu high-entropy alloy with an ultrafine-grained structure via friction stir processing, *Acta Metall. Sin. Engl. Lett.* 33 (7) (2020) 947–956.
- [37] A. Takeuchi, A. Inoue, Classification of bulk metallic glasses by atomic size difference, heat of mixing and period of constituent elements and its application to characterization of the main alloying element, *Mater. Trans.* 46 (12) (2005) 2817–2829.
- [38] D.B. Miracle, O.N. Senkov, A critical review of high entropy alloys and related concepts, *Acta Mater.* 122 (2017) 448–511.
- [39] N.N. Guo, L. Wang, L.S. Luo, X.Z. Li, Y.Q. Su, J.J. Guo, H.Z. Fu, Microstructure and mechanical properties of refractory MoNbHfZrTi high-entropy alloy, *Mater. Des.* 81 (2015) 87–94.
- [40] O.N. Senkov, C. Woodward, D.B. Miracle, Microstructure and properties of aluminum-containing refractory high-entropy alloys, *JOM* 66 (10) (2014) 2030–2042.
- [41] F. Otto, A. Dlouhy, C. Somsen, H. Bei, G. Eggeler, E.P. George, The influences of temperature and microstructure on the tensile properties of a CoCrFeMnNi high-entropy alloy, *Acta Mater.* 61 (15) (2013) 5743–5755.
- [42] H.Y. Yasuda, H. Miyamoto, K. Cho, T. Nagase, Formation of ultrafine-grained microstructure in Al_{0.3}CoCrFeNi high entropy alloys with grain boundary precipitates, *Mater. Lett.* 199 (2017) 120–123.
- [43] Y.L. Zhao, T. Yang, Y. Tong, J. Wang, J.H. Luan, Z.B. Jiao, D. Chen, Y. Yang, A. Hu, C.T. Liu, J.J. Kai, Heterogeneous precipitation behavior and stacking-fault-mediated deformation in a CoCrNi-based medium-entropy alloy, *Acta Mater.* 138 (2017) 72–82.
- [44] W. Guo, B. Liu, Y. Liu, T. Li, A. Fu, Q. Fang, Y. Nie, Microstructures and mechanical properties of ductile NbTaTiV refractory high entropy alloy prepared by powder metallurgy, *J. Alloy. Compd.* 776 (2019) 428–436.
- [45] H.W. Yao, J.W. Qiao, M.C. Gao, J.A. Hawk, S.G. Ma, H.F. Zhou, Y. Zhang, NbTaV-(Ti,W) refractory high-entropy alloys: experiments and modeling, *Mater. Sci. Eng. A* 674 (2016) 203–211.
- [46] H.W. Yao, J.W. Qiao, J.A. Hawk, H.F. Zhou, M.W. Chen, M.C. Gao, Mechanical properties of refractory high-entropy alloys: experiments and modeling, *J. Alloy. Compd.* 696 (2017) 1139–1150.
- [47] B. Liu, J. Wang, Y. Liu, Q. Fang, Y. Wu, S. Chen, C.T. Liu, Microstructure and mechanical properties of equimolar FeCoCrNi high entropy alloy prepared via powder extrusion, *Intermetallics* 75 (2016) 25–30.
- [48] S. Zhang, Z. Wang, H.J. Yang, J.W. Qiao, Z.H. Wang, Y.C. Wu, Ultra-high strain-rate strengthening in ductile refractory high entropy alloys upon dynamic loading, *Intermetallics* 121 (2020).
- [49] R. Sankalingam, S. Mishra, S.R. Cheethirala, V. Muthupandi, K. Sivaprasad, Enhanced relative slip distance in gas-tungsten-arc-welded Al_{0.5}CoCrFeNi high-entropy alloy, *Metall. Mater. Trans. A Phys. Metall. Mater. Sci.* 48A (8) (2017) 3630–3634.